Dynamical Features of a Biochemical Interaction in a Plant Root Hair Cell

A Long Story Short

Víctor F. Breña-Medina

Abstract In this chapter, we briefly discuss key dynamical features of a generalised Schnakenberg model. This model sheds light on the morphogenesis of plant root hair initiation process. Our discussion is focused on the plant called *Arabidopsis thaliana*, which is a prime plant-model for plant researchers as is experimentally well known. Here, relationships between physical attributes and biochemical interactions that occur at a sub-cellular level are revealed. The model consists of a two-component non-homogeneous reaction-diffusion system, which takes into account an on-and-off switching process of small G-protein family members called Rho-of-Plants (ROPs). This interaction however is catalysed by the plant hormone auxin, which is known to play a crucial role in many morphogenetic processes in plants. Upon applying semi-strong theory and performing numerical bifurcation analysis, all together with time-step simulations, we present results from a thorough analysis of the dynamics of spatially localised structures in 1D and 2D spatial domains. These compelling dynamical features are found to give place to a wide variety of patterns. Key features of the full analysis are discussed.

Keywords Plant root hair cell morphogenesis · Reaction-diffusion equations · Localised structure dynamics · Numerical bifurcation analysis · Nonlocal eigenvalue problems

1 Introduction

Morphogenesis is the biological process that organises growth, organisation and differentiation of the structure of an organism or parts of an organism. This process consequently gives rise to new life forms. That being so, a fundamental understanding of morphogenesis is vital for making advances across life sciences

---

V. F. Breña-Medina (✉)
Department of Mathematics, ITAMRío Hondo 1, Ciudad de México, Mexico
e-mail: victor.brena@itam.mx

L. Olivares-Quiroz, O. Resendis-Antonio (eds.), *Quantitative Models for Microscopic to Macroscopic Biological Macromolecules and Tissues*,
https://doi.org/10.1007/978-3-319-73975-5_10

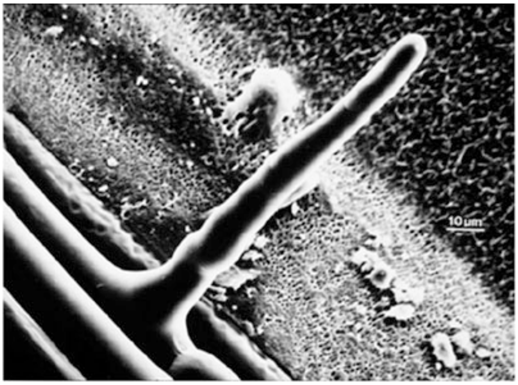

Fig. 1 A RH cell with a hair that is at $1/3$ of its final length. Figure reproduced from [1]

from agriculture up to human health. In agriculture for instance taking cognisance of flowering, self-pollination and nutrient uptake from the soil by plants, or *stem cells* specialisation and *apoptosis* can eventually help with crop yield or reforestation. For this reason, we will focus our discussion on the interplay between certain biochemical interactions in root hair plant cells and physical features as growth.

1.1 A Root-Hair Initiation Process

The majority of the surface area of the root system of a typical flowering plant is provided by its hairy outgrowths. Root hairs (RH)s are protuberances that outgrow from root epidermal surfaces. In *Arabidopsis*, these protuberances can grow up to more than 1 mm in length and approximately 10–20 µm in diameter, see Fig. 1. Thus the study of RHs is agriculturally important for understanding and optimisation of both nutrient uptake and anchorage. For instance, once humid soil is set, mineral salts and water can enter through plant roots. Higher densities of longer RHs are produced in regions where relatively low amounts of less mobile nutrients, such as phosphorus, are available. Roots grow through soil inducing a larger surface area between roots and soil. Consequently, a more advantageous absorption of nutrients is provided.

More widely, RH formation and growth in Arabidopsis has established itself as a key biological model problem within development and cell biology. This is mainly because RHs are found far from the plant body and become visible early in seedlings, so they are particularly amenable to scientific study due to the ease with which they can be imaged. In addition, the formation and growth of a RH represents an important problem in single-cell morphogenesis. Also, Arabidopsis is a model genetic organism for which there is an internationally coordinated project, providing large collections of mutants available for analysis, called *The Multinational Arabidopsis Steering Committee*. RHs grow quickly, at a rate of nearly 1 µm/min, allowing us to analyse efficiently the various phenotypes that arise under many different genetic mutations. Besides, a detailed analysis of the cellular changes can be experimentally tracked during the RH formation process, because their development is such that cells are organised in a single-file along the developing root epidermis. So young RH cells are found near the root tip and cells of increasing age and stage of growth are found further away in the same longitudinal stripe; see, for instance, [1] and the references therein.

Root hairs develop in predictable and organised files that allow detailed analysis during the whole process. Three different zones can be identified: the *meristematic zone* located in the root tip where new cells are formed in the *meristem*, which is covered by *root cap* cells; the *elongation zone*, where cellular expansion occurs, and the *differentiation zone* where RHs are produced.

Patterning information is provided at an early stage in epidermis development, immature epidermal cells destined to become RH cells are distinguished from their counterpart, non-RH cells, prior to hair outgrowth. The differentiating RH cells present a greater cell division rate, smaller length, greater cytoplasmic density, lower vacuolation rate and distinguishable cell wall epitopes; see, for instance, [2]. In addition, plant hormones known as *auxins* are thought to play a crucial role in almost all aspects of a plant's life. Auxins stimulate growth, and regulate fruit setting, budding, side branching, and the formation of delicate flower parts among many other morphogenic tissue-level responses. In a sense, RH outgrowth is one of the simplest and most easily studied effects that is stimulated by auxin. This hormone flows along the root from the core to the surface; see [3].

After being formed in the meristem, cells that will develop a RH become highly specialised. As the root continues to grow and the meristem moves away, the RH cells get wider, longer and deeper; this is done by diffuse growth, then the RHs form. This process can be divided into two main stages: *initiation*, when a small disc-shaped area of the cell is softened, gives rise to a swelling, and *tip growth*, when a protuberance grows by targeted secretion.

ROPs are examples of *Rho-family small GTPases*, a group of proteins whose role seems to be that of transmitting chemical signals in- and outside a cell in order to effect a number of changes inside the cell. Working as molecular "connectors", these proteins shift between active and inactive states. ROPs control a wide variety of cellular processes, they contribute strongly to crucial cellular level tasks such as morphogenesis, movement, wound healing, division and, of particular interest here, cell polarity generation; see, for example, [4]. These proteins are unique to plants, although are related to *Rac, Cdc42* and Rho-family small GTPases that control morphogenesis of animal and yeast cells, see [5] and the references within. In particular we are interested in the role of ROPs in forming patches that produce local cell outgrowths. That is, in the initiation stage, *small GTP-binding proteins* appear at the growth region. Exchange factor regulators *ARF GTPases* known as *ARF-GEFs* not only are inhibitors preventing ROP localisation, but also are required for the proper polar localisation of *PIN1*, a candidate transporter of the plant hormone auxin, see [6].

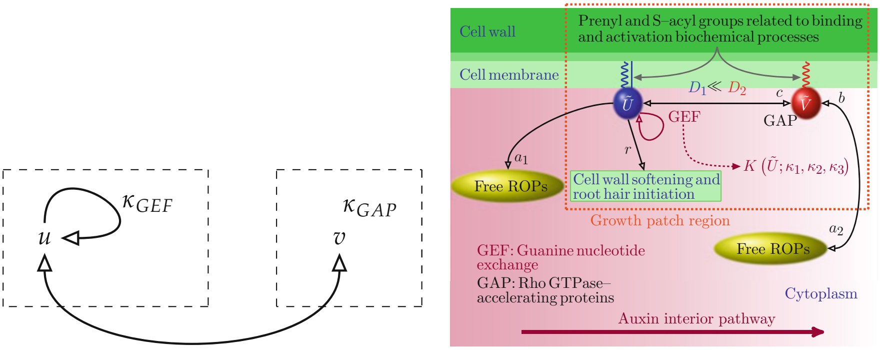

(a) (b)

Fig. 2 (**a**) Sketch of the switching fluctuation between active- and inactive-ROP densities. (**b**) Sketch of the model where autocatalytic activation and catalysis effect by auxin are coloured in purple. Figures reproduced from [8]

ROP localisation starts to produce a protuberance, at the same time the pH of the cell wall falls, which leads to softening of the cell wall where a hair is about to be formed. Moreover, plants overexpressing a mutant ROP that is permanently in the active form have balloon-shaped root hairs. On the other hand, protein *ROPGDI1* that can bind to the *GDP-bound* ROP and keep it in that form and in the cytoplasm has been inactivated. This suggests that ROPs are able to cycle from the *GTP-bound* form, which are attached to the cell membrane, to the GDP-bound form, which lie in the *cytoplasm*. In other words, ROPs switch between two states: active when are bound to GTP, and inactive when are bound to GDP, see [7]. The switching fluctuation between both active- and inactive-ROP forms is depicted below in Fig. 2a.

The biochemical process by which the process of RH formation is initiated within an Arabidopsis RH cell is depicted in Fig. 2b; blue and red balloons represent active-GTP ROP and inactive-GDP ROP respectively, ROPs which do not appear in the growth patch region (orange box) are represented by yellow balloons. Active-GTP ROP and Free ROP classes are able to transition to become either inactive-GDP ROP class or get unbound. This is illustrated by a double arrow connecting red and right-hand yellow balloons. A hypothesised autocatalytic process is symbolised by a purple loop-arrow attached to the active-GTP balloon. In addition, the green box encloses active-GTP class members that go to cell wall softening. Cell membrane binding activation processes are generally represented by snaking curves in blue and red accordingly. The interior auxin pathway is indicated by a purple arrow so the auxin gradient is represented by a decreasing purple shade in the same direction. As shall be seen further, we are interested in the binding process in the growth region.

A model of the initiation process was proposed by Payne and Grierson [9] in the form of a Schnakenberg-type reaction-diffusion system for inactive and active

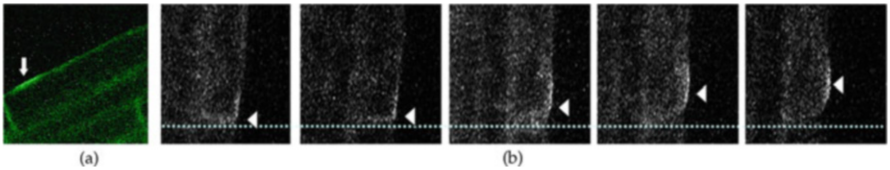

Fig. 3 (**a**) A patch of surface bound ROP imaged using GFP in wild-type just prior to cell wall bulging. Figure reproduced from [9]. (**b**) Time lapse of patch drift within a single cell from end-wall to wild-type location. Figure reproduced from [12]

ROPs. The key feature of the model is that the activation step is postulated to be dependent on the concentration of the plant hormone auxin. Auxin diffuses much faster than ROPs [10] and is too small to be imaged on its own and also very similar to the amino acid *tryptophan*, an essential component in many proteins which makes it impossible to make a sensor that is specific for auxin. However, Jones et al. [3] found a surprising difference between the location of auxin in- and out- pumps in RH and non-RH cells on the root epidermis. From this data, using the auxin flow model introduced by Kramer [11], Jones et al. were able to surmise that there is a decreasing gradient of auxin from the apical end of each RH cell.

Assuming that such a gradient mediates the autocatalytic activation of ROPs, simulations by Payne and Grierson showed that the active-ROP variable tends to form patch-like states towards the apical end, as in Fig. 3a. Moreover, various patch states can be found that show a close qualitative match with observations on the location, width and distribution of multiple hair cells in a variety of mutants.

Grierson et al. [12] presented the new experimental data reproduced in Fig. 3b which sheds light on the dynamic process by which ROP patches form. The process by which a patch of active ROP migrates from the apical cell boundary towards its wild-type position, from where a RH forms, takes place within a timescale of minutes. It appears to be triggered within the growing root as the RH cell reaches a combination of a critical length and a critical overall auxin concentration. In this review we shall present key results from the model derived by Payne and Grierson, which is particularly effective in capturing this dynamical process.

1.2 Fundamental Model

ROPs can become attached to the cell membrane through *prenylation* and *S-acylation*; these chemical modifications determine the steady-state distribution between the cell membrane and cytosol, the membrane interaction dynamics, as well as function [13]. In other words, each ROP protein comes in two states: activate and inactivate. The latter state corresponds to ROPs which may be either bound to the cell membrane or in the cytoplasm. Once bound though, there is a good chance of phosphorylation, leading to the active form of ROP. In the model here derived we shall not model the binding mechanism per se but shall differentiate only between the active form which can only diffuse within the confines of the cell membrane, and the inactive form, the majority of which is free to diffuse in the cytoplasm. We will also approximate the long-thin RH cell by a domain (either 1D or by a rectangular domain in 2D with high aspect ratio), and shall distinguish between membrane and cytoplasm only through separate diffusion constants, D_1 and D_2 for the active-ROP and inactive-ROP populations, respectively. That is, we model a mathematical domain $(\mathbf{z}, t) \in \Omega^d \times \mathbb{R}^+ \cup \{0\}$, which Ω^d is either the interval $\Omega \equiv [0, L]$ or the rectangle $\Omega^2 \equiv [0, L_x] \times [0, L_y]$ where $L_x > L_y$, and let $u(\mathbf{z}, t)$ represent the concentration of *bound/active* and $v(\mathbf{z}, t)$ the *unbound/inactive* ROP. In the model we shall also reflect the fact that the kinetic processes occur considerably faster than the changes to cell length and auxin concentration levels. Therefore we shall assume that the latter are effective bifurcation parameters that vary quasi-statically.

The active Rho state is assumed to be deactivated at rate κ_{GAP}, and equivalently the inactive Rho state is activated at rate κ_{GEF} depending upon the presence of GEFs or GAPs, respectively; see sketch in Fig. 2b.

To derive a specific form for the activation and deactivation steps we shall take a model that is inspired by similar processes for Rho proteins in mammals and yeast. There, it is widely held that the GEF activation step involves positive feedback (autocatalysis) whereas the GAP step is thought to be passive; see, for example, [7]. Both Jilinke et al. [14] and Otsuji et al. [15] have derived models for active process of cross-talk between the three different mammalian/yeast Rhos—*cdc42, RhoA* and *Rac*—which process is thought to underlie the polarity determination process. Like ROPs, each protein is supposed to come in two states, an activated state (which is bound to the cell membrane) and a deactivated state (either bound or in the cytosol). Similarly the transition between these two states is via GEFs and GAPs. In [14, 15], the GEF-induced activation step of each Rho species is modelled by a Hill function:

$$\kappa_{\text{GEF}}(u) \equiv \kappa_1 + \frac{\kappa_2 u^q}{1 + \kappa_3 u^q}, \tag{1}$$

where κ_1 is the activation rate, κ_2 represents autocatalytic acceleration, κ_3 is a saturation coefficient, and the power q is typically taken to be an integer but need not be. In [14, 15] the typical value $q = 2$ is chosen which preserves the odd power of the nonlinearity in their models. This may be simplified as follows. In plants, although there are several different kinds of ROP, their activation is not thought to involve cross talk. Also, by including a constant production rate of the inactive ROP and a constant probability of recycling or further processing of active ROP, there is no need for an explicit saturation term, which implies that κ_3 can be set to naught; see proposed model in [9].

As we previously referred, Jones et al. [3] found experimental evidence that suggests a longitudinal spatially decaying gradient of auxin which Payne and Grierson postulate modulates the autocatalytic step. That is, we suppose then the parameter κ_2 is spatially dependent: $\kappa_2 = k_{20}\alpha\left(\mathbf{z}; \left|\Omega^d\right|\right)$. Here k_{20} measures an

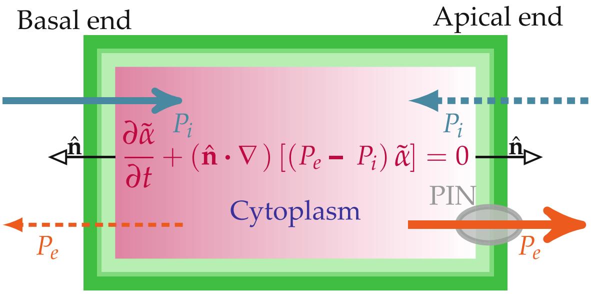

Fig. 4 Sketch of the auxin flux in the RH cell; azimuthal view. The gradient is coloured as a purple shade. Cell wall and cell membrane are coloured as in Fig. 2b. Figure reproduced from [8]

overall concentration of auxin and, as is sketched in Fig. 4, $\alpha\left(\mathbf{z}; \left|\Omega^d\right|\right)$ is a smooth function that represents the spatial distribution of auxin, normalised so that

$$\alpha(0, y) = 1, \qquad \frac{\partial\alpha}{\partial x} < 0, \quad \text{for all } \mathbf{z} \in (0,1)\times(0,1)\,, \text{where} \mathbf{z} = (x, y)\,. \tag{2}$$

In contrast, we suppose that $\kappa_1 = k_1$ a constant. All other processes are supposed to follow the simple law of mass action, with the GEF-induced deactivation/unbinding rate given by a constant $\kappa_{\mathrm{GAP}} = c$. Furthermore, b is assumed to be the constant rate of production of inactive ROP and r the rate at which active ROP is recycled or used up to produce other complexes, including those that go on to produce cell wall softening; see Fig. 2.

On the other hand, for the 2D case, we take into account two different scenarios:

$$\alpha(\mathbf{z}) = e^{-\nu x}\sin(\pi y) \quad \text{and} \quad \alpha(\mathbf{z}) = e^{-\nu x}\,. \tag{3}$$

Under the above assumptions, using the law of mass action allied to Fick's law of diffusion in a standard way, we obtain the reaction-diffusion (RD) system of equations

$$\text{Bound} - \text{activeROP}: \quad U_t{=}D_1\Delta U{+}k_{20}\alpha\left(\mathbf{z}; \left|\Omega^d\right|\right)U^2V{-}(c{+}r)U{+}k_1V\,, \tag{4a}$$

$$\text{Unbound} - \text{inactiveROP}: \quad V_t = D_2\Delta V - k_{20}\alpha\left(\mathbf{z}; \left|\Omega^d\right|\right)U^2V + cU - k_1V + b\,, \tag{4b}$$

in Ω^d. We also impose the homogeneous Neumann boundary conditions, also known as no-flux boundary conditions,

$$\frac{\partial U}{\partial\hat{\mathbf{n}}} = 0, \quad \frac{\partial V}{\partial\hat{\mathbf{n}}} = 0\,,$$

on $\partial\Omega$, which supposes that the large ROPs do not diffuse through the cell wall.

This system is a generalisation of the Schnakenberg model [16], which is doubtlessly one of the most widely studied models undergoing Turing-like pattern formation schemes. In contrast to other models such as the *Brusselator* [17], which takes into account four chemical reactions, the Schnakenberg one is a simplification where three hypothetical chemical reactions are represented, amongst which one is autocatalytic. As a consequence, it is not only simpler, but also it is already known that the Schnakenberg system can display features that are considered biologically relevant [16]. The usual Schnakenberg system can be obtained from (4) by setting k_1 and c to zero, adding a constant production term to the u-equation, and taking $\alpha \equiv 1$; this transformation can be seen as a homotopy between both systems. Furthermore, both systems are derived from simple reactions where an autocatalytic process is present. In addition, as can be straightforwardly explored, both describe activator-substrate processes. In other words, near activation regions the activator u aggregates so that the substrate v is consumed quickly, as a result substrate valleys occur where activator peaks do; see [18] and the references therein for a review.

From a theoretical point of view there is an extensive range of research on the Schnakenberg model. For instance, Ward and Wei have analysed existence and asymmetry of spikes [19]; stability of symmetric N-spiked steady-states is deeply examined in [20]; self-replication spots and their dynamics in 2D are studied in [21]; and for findings on chemical reactors, see, e.g., [22], where this model plays a central role.

In non-homogenous approach, there has been mathematical analysis in super-conductivity (e.g. [23]). Reaction-diffusion equations with spatially dependent coefficients of nonlinear terms are not easy to study analytically, see, e.g., [24]. Nevertheless there have been some previous works both analytical and numerical: for the Schnakenberg system, see, e.g., [25], the Gierer–Meinhardt and Brusselator systems (e.g. [26]), and in models of mitosis in cytokinesis [27]. In this essay we present central results of the Schnakenberg-like system (4) with spatially dependent coefficients which modulate the nonlinear terms.

This chapter is organised as follows: in Sect. 2, the onset of spatially localised structure in RD systems from a Turing perspective is briefly examined; dynamical features observed as auxin is switched on are addressed in Sect. 3; in Sect. 4, a natural transition from a 1D domain to a 2D domain is then briefly presented from a point of view of localised stripe stability analysis; then, geometrical and kinetics characterisation of spot dynamics, along with hybrid patterns consisting of spot and stripes, are reviewed when a two-dimensional spatially dependent gradient is on in Sect. 5. Finally, concluding remarks are found in Sect. 6. All key results on pattern formation dynamics and inherent instabilities on RH-initiation morphogenesis presented here are discussed in [8, 28–31].

2 Spatially Localised Activator Structures

As can be seen in Fig. 3, there are two main features which may be addressed from a viewpoint of the theory of dynamical systems: (1) ROP aggregation and (2) ROP patches drifting. The former seems to occur in such a way that, from an analytical point of view, active-ROP patches have a spatially localised structure. On the other hand, in contrast to patch formation, once formed active-ROP patches slowly shift from the basal end towards interior of the cell. This observation suggests that both mechanisms, aggregation and drifting, arise in two different time scales.

2.1 Turing and Homoclinic Snaking

First of all, U and V components are renamed as u and v, respectively. Without loss of generality, no spatially dependent auxin gradient and a large symmetrical 1D domain are taken into account. In so doing, we set $\alpha \equiv 1$, $k_{20} \equiv k_2$ and $\Omega \equiv [-L/2, L/2]$ for $L \gg 1$, together with homogeneous Neumann boundary conditions.

On the one hand, we first look for Turing patterns, which are known to emerge from pitchfork (breaking-symmetry) bifurcations. As a consequence, upon following a standard approach, necessary conditions to get non-trivial steady-states can be encapsulated by

$$D_1 D_2 \ll \max\left\{D_1^2, D_2^2\right\}\,, \quad \operatorname{sign}\{\, F_u G_v\} < 0\,.$$

Assuming, for instance, that $G_v < 0$, conditions above imply that u-component diffuses much slower than v-component; see [32] for details. As can be seen there, a flat steady-state transits to a non-trivial steady-state as a parameter is slowly varied. In particular, this transition materialises when a double zero of the dispersion relation occurs. In other words, condition

$$(D_2 J_{11} + D_1 J_{22})^2 = 4 D_1 D_2 \det \mathbf{J}\,, \quad (\mathbf{J})_{ij} = J_{ij}\,, \tag{5}$$

is satisfied, where $\mathbf{J}$ is the Jacobian matrix of kinetic terms of system (4) at the steady-state

$$(u_0, v_0)^T = \left(\frac{b}{r}, \frac{br(c+r)}{k_2 b^2 + r^2 k_1}\right)^T\,. \tag{6}$$

Furthermore, condition (5) corresponds to an accumulation point of Turing bifurcations when $L \gg 1$.

On the other hand, in the limit $L \to \infty$, spatial dynamics can be applied (see, e.g., [33]). Hence, upon setting $u_t = v_t = 0$ we obtain the steady-state system, which is equivalent to an ODE system in $\mathbb{R}^4$,

$$u_x = \frac{p}{D_1}\,, \qquad p_x = -k_2 u^2 v + (c+r)u - k_1 v\,, \tag{7a}$$

$$v_x = \frac{q}{D_2}\,, \qquad q_x = k_2 u^2 v - cu + k_1 v - b\,. \tag{7b}$$

Notice that this system satisfies two key ingredients: (a) spatial translation invariance and (b) spatial reversibility, which corresponds to the symmetry $(u_x, v_x)^T \to (-u_x, -v_x)^T$ and $x \to -x$. In this context, the steady-state $(u_0, v_0)^T$ of (4) corresponds to an equilibrium $(u_0, 0, v_0, 0)^T$ of (7), which will undergo a transition from being hyperbolic to elliptic equilibrium at a Hamilton–Hopf bifurcation. This bifurcation takes place when eigenvalues of the Jacobian matrix at the equilibrium of (7) collapse into two purely imaginary eigenvalues of multiplicity two for a critical parameter value, which is however found when the same condition (5) is met. In addition, as can be seen in [34], a subcritical Hamilton–Hopf bifurcation is essential to get spatially localised steady-states, which are equivalent to homoclinic orbits for system (7). As a consequence, a subcritical Turing bifurcation plays a key role on the onset of spatially localised structures.

Upon applying the Lyapunov–Schmidt reduction method, we compute the reduced bifurcation equation

$$g(\chi, \mu) = q_1 \mu \chi + q_3 \chi^3 + q_5 \chi^5 + \mathcal{O}(\mu^2 \chi, \mu \chi^3)\,,$$

where $\mu = k_2 - k_{2_c}$ and $\chi \in \mathbb{R}$ parametrises eigenfunctions amplitude of $\mathbf{J}_\kappa$. This matrix is the Jacobian matrix of (4) at the steady-state $(u_0, v_0)^T$, restricted to the eigenspace spanned by cosine Fourier modes; see [8] for details. Bifurcation algebraic structure is provided by equation $g(\chi, \mu) = 0$. From which a criticality transition is predicted as k_2 is slowly varied. That is, criticality parameter $\sigma \equiv q_1 q_3$ predicts a sub- or supercritical pitchfork bifurcation as $\sigma > 0$ or $\sigma < 0$, respectively; see Fig. 5b.

Spatially localised steady-states are then organised in a homoclinic snaking fashion. This form emerges from a subcritical pitchfork bifurcation close to criticality transition. As can be seen in Fig. 5c, stable branches are flanked by fold bifurcations; as a result, stable branches overlap.

Therefore, a subcritical Turing bifurcation is the onset of localised steady-states, which co-exist with spatially extended non-trivial steady-states. Samples of system (4) stable patterns in 1D are displayed in Fig. 5d. On the other hand, stable patterns for a 2D square large domain are shown in Fig. 6. These solutions suggest that a similar mechanism governs such a localised patterns in 2D. See [28, 35] for a detailed discussion.

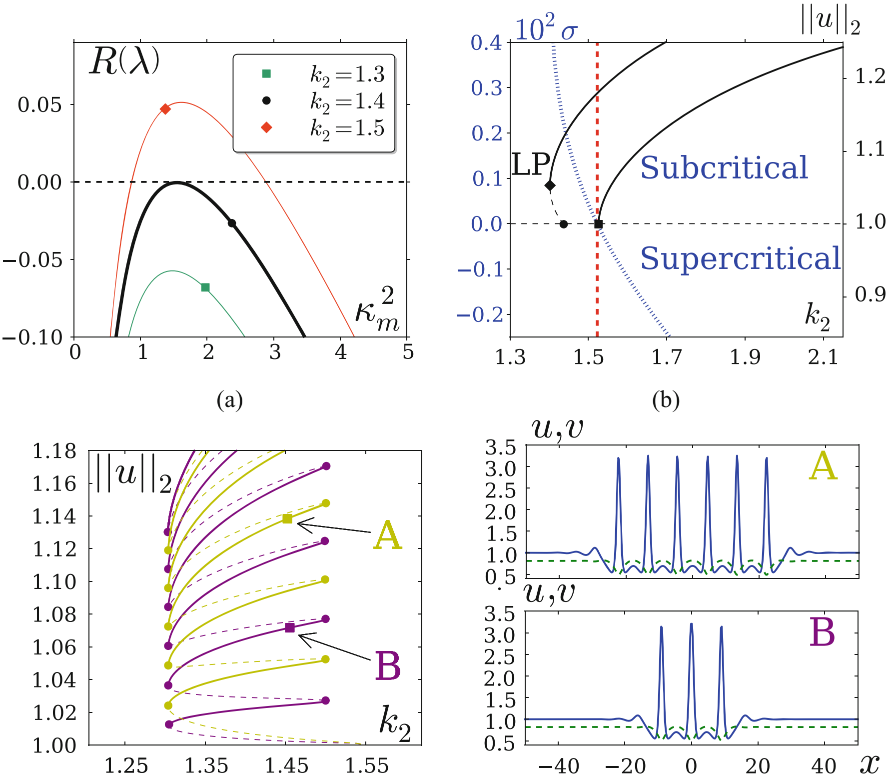

(a) (b)

(c) (d)

Fig. 5 (**a**) Dispersion relation of $\mathbf{J}_\kappa$; $\kappa_m^2 = m\pi/L$ for $m \in \mathbb{Z}$. The bold solid curve corresponds to where a double root occurs. (**b**) Bifurcation diagram and pitchfork criticality condition; stable branches are shown as solid lines, the filled circle corresponds to a subcritical bifurcation, and the square to a supercritical bifurcation. The subcritical branch undergoes to a fold bifurcation (LP). The pitchfork criticality condition is depicted as a blue heavily dashed line, where the criticality transition is indicated by a red vertical dashed line. (**c**) Homoclinic snaking; even-solutions branch in yellow and odd-solutions branch in purple, and fold bifurcations depicted as filled circles; bold solid lines indicate stable branches. (**d**) Samples of multi-pulse homoclinic stable solutions on the even and odd branch for $k_2 = 1.45$, top and bottom panels, respectively, which correspond to six-spike steady-state (label A) and three-spike steady-state (label B) in panel (**c**). The u-component (blue solid line) and v-component (green dashed line) are plotted. Figures reproduced as well as parameter values from [28]

3 Spatially Dependent Gradient

In order to understand auxin catalyst properties on ROP activation, an auxin gradient as stated in (2) is taken into account. For a 1D domain, this gradient though is as the right-hand scenario in (3) with no transversal component. In addition, as RH cells are still growing at this initiation stage, length seems to also play an important role

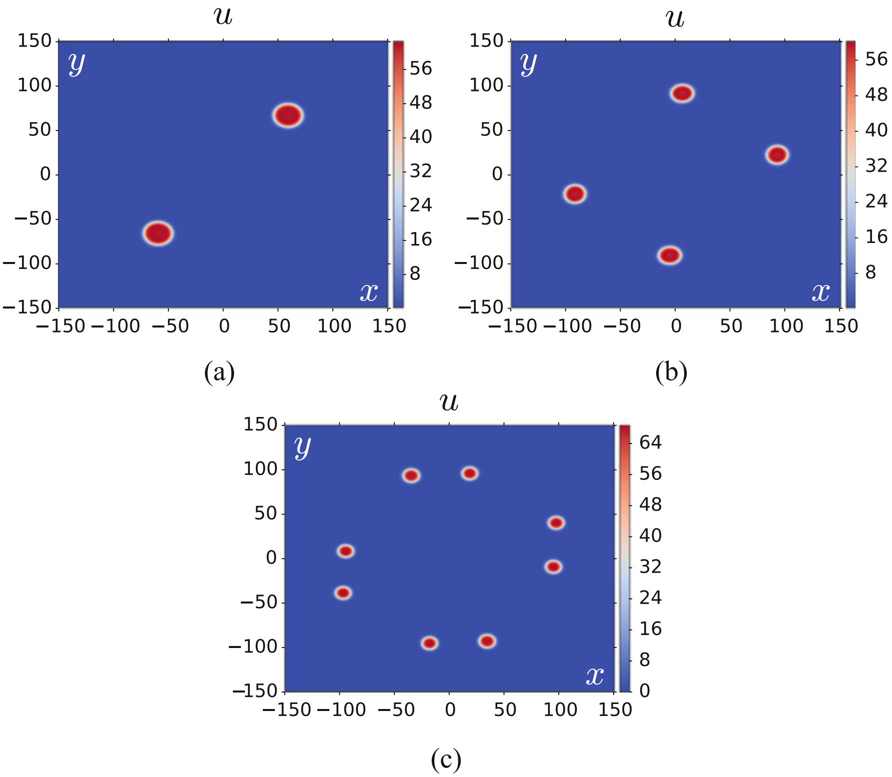

(a)

(b)

(c)

Fig. 6 Stable patterns for a 2D square domain on a cool-warm scale (sidebar). Localised (**a**) two-spot, (**b**) four-spot, (**c**) eight-spot. Figures reproduced as well as parameter values from [28]

in active-ROP pattern formation. Upon taking into account these two ingredients, auxin accelerator rate is $\kappa_2 = k_{20}\alpha(x)$, where k_{20} plays a role as the primary bifurcation parameter, and $\Omega = [0, L]$, where L is a secondary bifurcation parameter.

In so doing, we perform time-step simulations of system (4) for different auxin overall k_{20} values. Initial conditions consist of a random perturbation of order 10^{-4} to steady-state (6). As can be seen in Fig. 7, spikes are quickly formed which then slowly drift towards interior of the domain. In addition, an asymmetrical amplitudes and a travelling-wave-like spikes get pinned closer to left-hand boundary can be observed. These numerical observations suggest: (1) families of stable steady-states arranged in an overlapping bifurcation structure, and (2) two time scales and two spatial scales.

As seen in Sect. 2, upon varying k_{20} a subcritical bifurcation is perturbed and compute the bifurcation diagram shown in Fig. 8a. There, stable branches and unstable branches are flanked by fold bifurcations, which are organised in an overlapping fashion. This is a consequence of a strongly slanted homoclinic-snaking structure previously computed above. Note that as the k_{20} is greater, the more

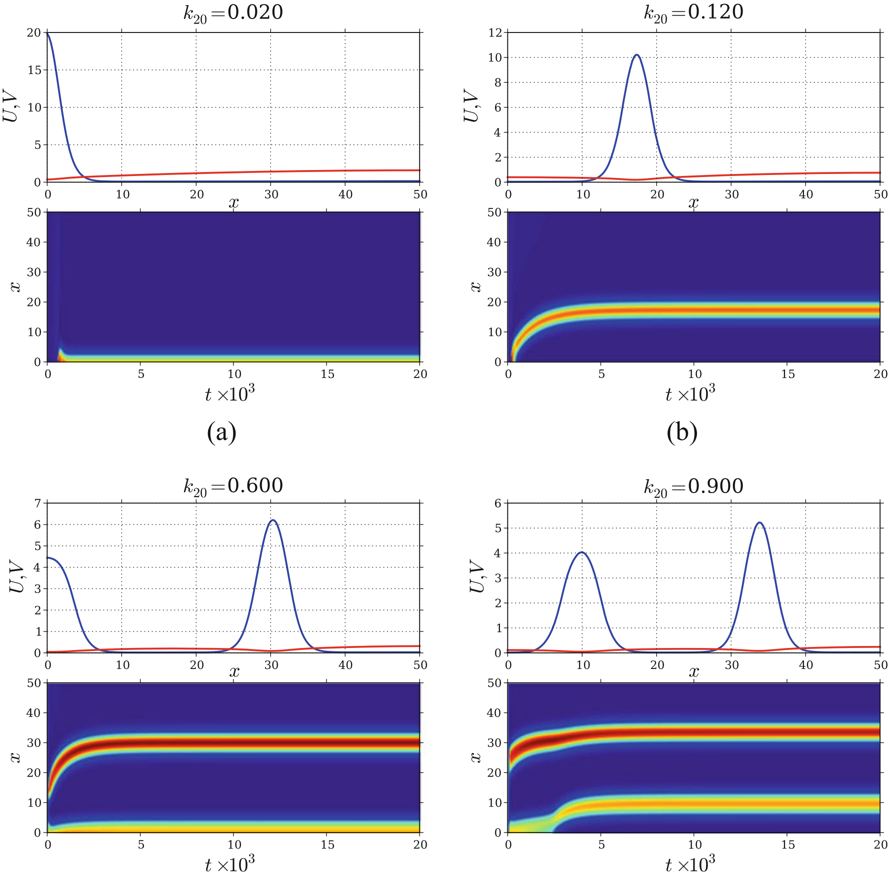

(a) (b)

(c) (d)

Fig. 7 Final profile and patch dynamics, with no variation of parameters, for (**a**) boundary patch, (**b**) an interior patch, (**c**) double patch, and (**d**) boundary and interior patch. Active- and inactive-ROP density final profiles are plotted in blue and red, respectively (top panels), and u-spike solutions are plotted on a heat bar scale (bottom panels). Figures reproduced as well as parameter values from [29]

spikes arise, which implies that auxin triggers high active-ROP densities in localised regions. Notice that the closer to the left-hand boundary, the smaller amplitude occurs.

Now, spatio-temporal scales are in such way that spikes are formed in a fast time scale to then travel towards a steady location in a slow time scale, and the two spatial scales can be seen as inner and outer scales of each spike. This approach can be seen as a Dirac-delta function works as each spike core. That is, spikes are flat in the outer scale and finite but large in the inner scale; see Fig. 8b.

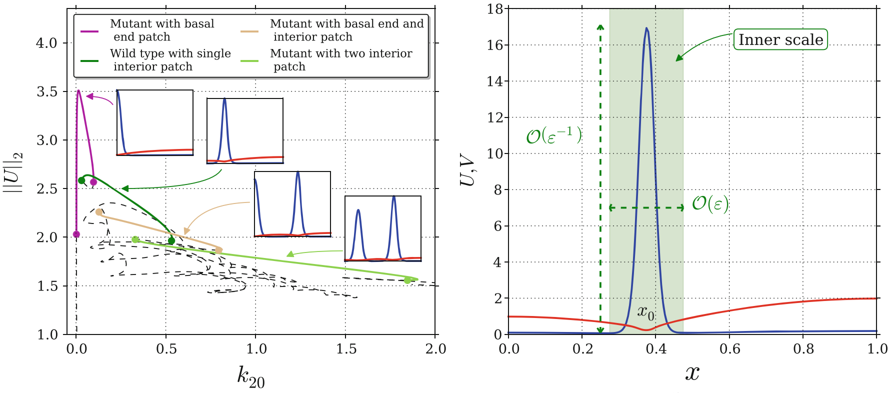

(a) (b)

Fig. 8 (**a**) Bifurcation diagram varying k_{20}: boundary-patch, single-interior-patch, boundary-and-interior- patch, and two-interior-patch branches; stable solutions are shown as solid lines, unstable solutions as dashed lines, and points instability points by filled circles. (**b**) Schematic plot of the inner and outer solution for a steady-state solution. The active-component U has a patch, whereas V has a global variation across the domain. Figures reproduced as well as parameter values from [29]

Upon re-scaling $U = \varepsilon^{-1}u$ and $V = \varepsilon v$, where $u, v = \mathcal{O}(1)$, we obtain a singularly perturbed system

$$u_t = \varepsilon^2 u_{xx} + \alpha(x)u^2 v - u + \frac{\varepsilon^2}{\tau\gamma}v\,, \tag{8a}$$

$$\varepsilon\tau v_t = D_0 v_{xx} + 1 - \varepsilon v - \varepsilon^{-1}\left(\tau\gamma\left(\alpha(x)u^2 v - u\right) + \beta\gamma u\right)\,, \tag{8b}$$

in $0 < x < 1$ and $t > 0$, with $u_x = v_x = 0$ at $x = 0, 1$, and $D_0 \equiv \varepsilon D$ which comes from balancing terms in (8b).

Here, the dimensionless parameters are given by

$$\varepsilon^2 \equiv \frac{D_1}{L^2(c+r)}\,, \qquad D \equiv \frac{D_2}{L^2 k_1}\,, \qquad \tau \equiv \frac{c+r}{k_1}\,, \qquad \beta \equiv \frac{r}{k_1}\,, \tag{9}$$

and the primary bifurcation parameter is

$$\gamma \equiv \frac{(c+r)k_1^2}{k_{20}b^2}\,. \tag{10}$$

By applying matched asymptotic method in system (8), we obtain a U and V leading order approximation profiles as stated by

Proposition 3.1 (Modified Version from [29]) *Let* $\varepsilon \ll 1$, $D = \mathcal{O}(\varepsilon^{-1})$ *with* $D = D_0/\varepsilon$ *and* $\gamma = \mathcal{O}(1)$, *and consider an* $N + 1$ *interior patch quasi-steady-*

state solution of (8) *with patches centred at* $x_0, \ldots, x_N$. *Then, a leading order approximation for U and V is*

$$U \sim \frac{\varepsilon^{-1}}{6\beta\gamma} \sum_{j=0}^{N} w\left(\varepsilon^{-1}(x - x_j)\right) n_j \,, \tag{11a}$$

$$V \sim \varepsilon \left(6\beta\gamma(N+1)\bar{\alpha}_{-1} - \mathbf{n}^T\mathbf{G}\mathbf{n} + \sum_{j=0}^{N} G\left(x; x_j\right) n_j \right) , \tag{11b}$$

where $w(\xi) = 3/2\text{sech}^2\,(\xi/2)$, $G(x; x_j)$ *is a Green function, and*

$$\bar{\alpha}_{-1} \equiv \frac{1}{N+1}\left[\frac{1}{\alpha(x_0)} + \cdots + \frac{1}{\alpha(x_N)}\right] .$$

Here $\mathbf{n} = (n_0, \ldots, n_N)^T$ *is the solution to the nonlinear algebraic system*

$$6\beta\gamma\mathbf{B}\mathbf{n}_{-1} = \mathbf{G}\mathbf{n} + 6\beta\gamma(N+1)\bar{\alpha}_{-1}\mathbf{e} - \left(\mathbf{n}^T\mathbf{G}\mathbf{n}\right)\mathbf{e} \,, \quad \mathbf{e} \equiv (1, \ldots, 1)^T \,, \tag{12}$$

where $\mathbf{B} \equiv \text{diag}\left(\alpha\left(x_0\right), \ldots, \alpha\left(x_N\right)\right)$, *and symmetric Green's matrix* $\mathbf{G}$ *is defined by* $(\mathbf{G})_{ij} = G(x_i; x_j)$. *In terms of* n_i, *the leading-order solution for V in the vicinity of the i-th patch is* $V^i \sim 6\varepsilon\beta\gamma/\alpha(x_i)n_i$.

As can be seen, each amplitude of active-ROP spike is governed by means of n_j, which depends on auxin gradient as the nonlinear algebraic system (12) indicates; see Figs. 7 and 8a for amplitude asymmetries. Moreover, V approximation consists of the Green's matrix and regulating constants n_j, which implies that boundary conditions and interactions between spikes are mediated by inactive-ROP density. In other words, localised biochemical activation is controlled by auxin; however, geometry and growth factors indirectly determine shape and form of the pattern influence through inactive-ROPs. For full details of other dynamical features not shown here and a complete analysis, see [29].

4 Geometrical Key Role

In the previous section, key features of a two-component RD system in a 1D domain were described to model a RH initiation process catalysed by auxin in a slim and flat RH cell. In so doing, as symplastic auxin flow actively diffuses from RH cell to RH cell, we have only considered a longitudinal spatially dependent gradient. However, non-RH cells are known to flank RH cells. This characteristic has been taken into account by Grieneisen et al. in [36]. From their model, a transversal auxin gradient may be assumed to have impact on active-ROP pattern formation and patches location dynamics. In order to analyse this feature on ROP dynamics, a 2D domain is now considered. Such a domain provides a setting with an extra degree of freedom. Hence, we address the following questions:

- How would RH width affect ROP pattern formation?
- Would a robust ROP patch formation be able to arise as seen in 1D?
- Which spatial aggregation structure would active-ROPs have in 2D?
- Are there other kind of patterns co-existing with localised patterns?

We first notice that Proposition 3.1 provides a key ingredient. That is, upon denoting spike steady-states (11) as $(u_s(x), v_s(x))^T$, and as the auxin gradient is considered to be y-constant, these states in 1D are also stripe steady-states $(u_s(x; y), v_s(x; y))^T$ in 2D, where transversal direction is parametrised by y. Expressed in a different way, transversal trivial extensions of stationary spike solutions give form to stationary stripe solutions; these stripes are known as *homoclinic stripes* (cf. [37]), see Fig. 9. This homoclinic stripe is constructed by a 1D spike (bold solid curve) pinned at $x_0(\eta; \gamma)$, which gets located in the slow time $\eta = \varepsilon^2 t$ for a fixed γ value. Then, it is transversally extended. As a consequence, a stripe flanked by bold solid curves is obtained.

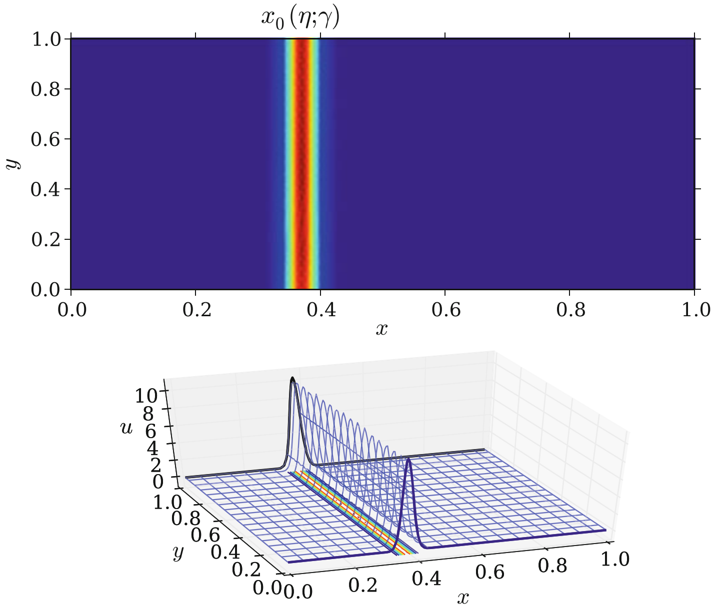

Fig. 9 Homoclinic stripe on a heat scale in the upper panel. In the bottom panel, spikes (bold solid blue curves) at $x_0(\eta; \gamma)$ correspond to stripe ends. This stripe comes from a trivial extension of a 1D spike

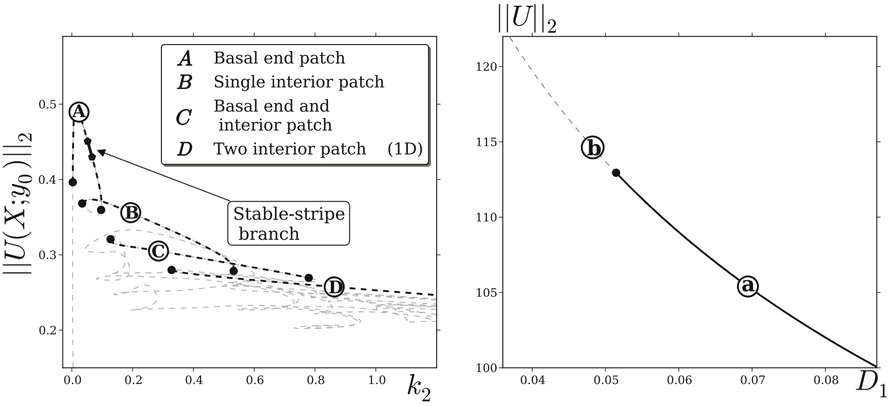

(a) (b)

Fig. 10 (**a**) Comparison of bifurcation diagrams between localised stripes and 1D-spike scenarios. Bold dashed portions of the diagram indicate where stable 1D solutions are unstable to transverse instabilities. A narrow stable window is found, given by the solid black curve. (**b**) Bifurcation diagram as D_1 varies from a solution in stable-stripe branch shown in (**a**). An eigenvalue crosses into the right-hand complex semi-plane at the filled black circle. Branch labelled by **a** remains stable as D_1 is increased further (not shown). Figures reproduced as well as parameter values from [30]

In dimensionless form the model is posed on a square $(x, y) \in \Omega^2 \equiv [0, 1]\times[0, 1]$, which has been rescaled from a rectangular domain $\Omega^2 \equiv [0, L_x]\times[0, L_y]$ and aspect ratio $s = (L_x/L_y)^2$, so that in (4) we have allowed for a Laplacian defined as $\Delta \equiv \partial_{xx} + s\partial_{yy}$. As a consequence, we get a bifurcation diagram which has the same structure as bifurcation diagram in Fig. 8a, but stability is drastically changed; see Fig. 10a. We use the L_2-norm of the active component for a fixed value of y as a solution measure. We find patterns with one boundary stripe (A), one interior stripe (B), one boundary and one interior stripe (C), and two interior stripes (D). All the solution branches, apart from a small segment (bold line), are unstable. The stable extended pattern branch (solid black curve ends in Fig. 10a) becomes unstable as D_1 decreases. This gives an insight on the asymptotic limit, i.e. sharper boundary stripes are unstable. To shed light on this, upon selecting a solution from the stable stripe-branch as initial condition, we perform continuation on D_1. As can be seen in Fig. 10b, there is a small critical value at which boundary stripe solutions become unstable.

To rigorously prove that stripes are unstable, semi-strong theory is used to derive a nonlocal eigenvalue problem (NLEP). From Proposition 3.1 for $N = 0$, a stationary stripe solution is substituted into system (8), and upon considering a localised eigenfunction for the active component, we obtain

Proposition 4.1 (Modified Version from [30]) *The stability on an $\mathcal{O}(1)$ time-scale of a quasi steady-state interior stripe solution of (8) is determined by the spectrum of the NLEP*

$$\mathcal{L}_0\Phi_0 - \theta_h(\lambda;m)\, w^2\, \frac{\int_{-\infty}^{\infty} w\Phi_0\, d\xi}{\int_{-\infty}^{\infty} w^2\, d\xi} = \left(\lambda + s\varepsilon^2 m^2\right)\Phi_0\,, \tag{13}$$

$$-\infty < \xi < \infty\,; \quad \Phi_0 \to 0\,, \quad as \quad |\xi| \to \infty\,,$$

where Φ_0 is the localised eigenfunction at the leading order, $\mathcal{L}_0\Phi_0 \equiv \Phi_{0\xi\xi} - \Phi_0 + 2w\Phi_0$, and $\theta_h(\lambda;m)$ is given by

$$\theta_h(\lambda;m) \equiv \mu\left(\frac{\lambda + 1 + s\varepsilon^2 m^2 - 2\kappa}{\lambda + 1 + s\varepsilon^2 m^2 - \mu\kappa}\right)\,, \tag{14}$$

$$\mu \equiv 2\left[1 + \frac{D_0}{6\chi G^0}\right]^{-1}\,, \qquad \chi \equiv \frac{\tau\alpha\,(x_0)}{36\beta^2\gamma}\,, \qquad G^0 \equiv G\,(x_0;x_0)\,.$$

Here $G\,(x;x_0)$ is defined by

$$G_{xx} - sm^2 G = -\delta\,(x - x_0)\,, \quad 0 < x < 1\,;$$
$$G_x(0;x_0) = G_x(1;x_0) = 0\,; \qquad [G_x]_{x_0} = -1\,,$$

and the wavenumber m in the y-direction is $m = \pi k$ with $k \in \mathbb{Z}^+$.

From (13), a dispersion relation is formally found to be as shown in Fig. 11. This comes from the fact that there exist two roots of $\Re(\lambda)$ at m_{low} and m_{up}, which implies

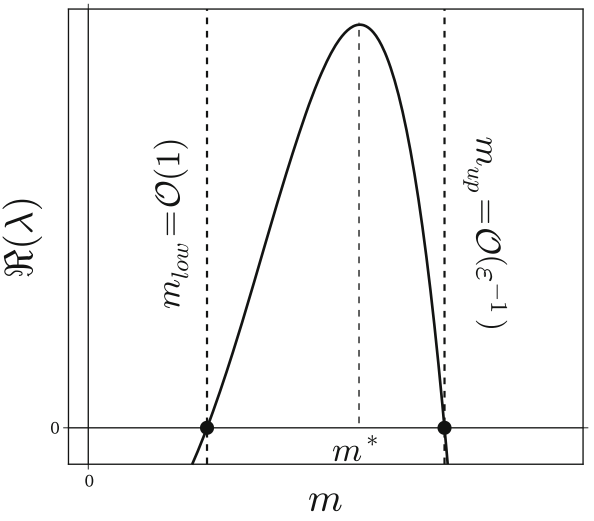

Fig. 11 Sketch of a dispersion relation $\Re(\lambda)$ versus m, showing the unstable band of wavenumbers lying between the vertical dashed lines. The expected number of spots is closely determined by the most unstable mode m^*. Figure reproduced from [30]

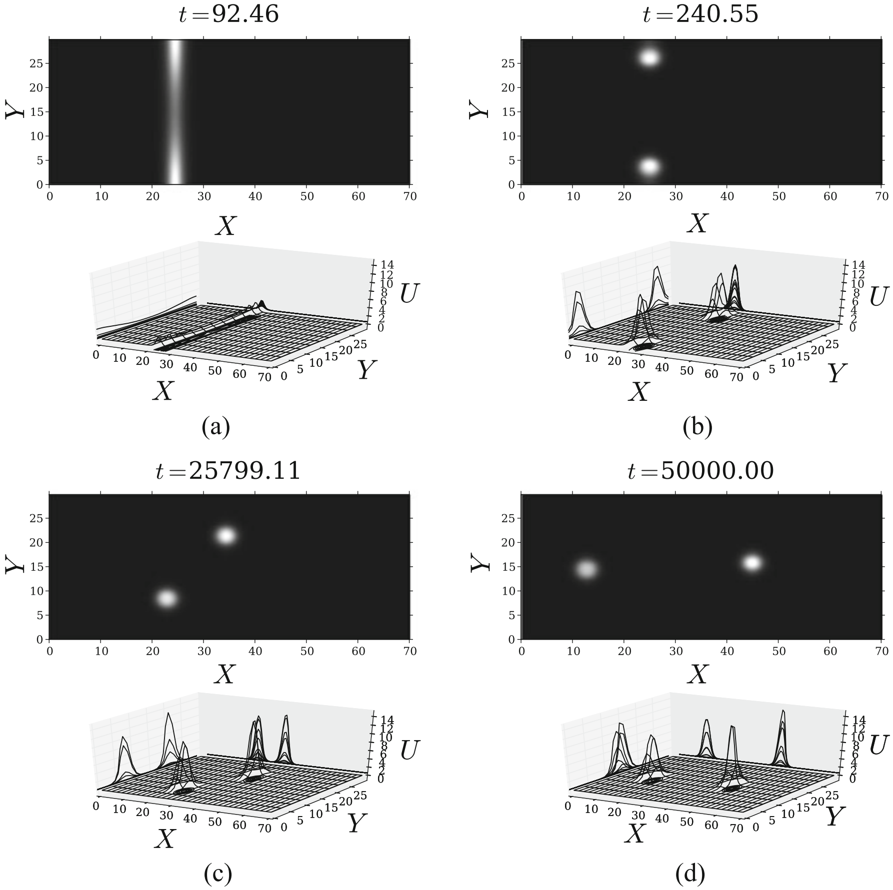

Fig. 12 Breakup instability and secondary $\mathcal{O}(1)$ time-scale instabilities of an interior localised stripe for U. (**a**) The localised stripe initially breaks into two spots; (**b**) once formed, the spots migrate from the boundary towards each other along the x-location line, and (**c**) rotate until they get aligned with the longitudinal direction. (**d**) Finally, they get pinned far from each other. Figures reproduced as well as parameter values from [30] with $k_2 = 0.5$, which corresponds to a stripe location at $x_0 = 24.5$

that there will be always a band of unstable transversal modes m. The most unstable mode m^* determines the number of spots the stripe will break up. For $s = 5.5$ and relative stripe location $x_0 = 0.35$, the dispersion relation (not shown) computed from (13) predicts that an interior stripe break up into either two or three spots. An interior stripe is taken as the initial condition and perform a direct numerical simulation of the full PDE system (4). The results are shown in Fig. 12, where we observe from Fig. 12a and b that the stripe initially breaks into two distinct localised spots. The spatial dynamics of these two newly-created spots is controlled by the auxin gradient. They initially move closer to each other along a vertical line, and then rotate slowly in a clockwise direction to eventually become aligned with the horizontal direction associated with the auxin gradient $\alpha(x)$ (see Fig. 12c). Finally, in Fig. 12d we show a stable equilibrium configuration of two spots lying along the centre line of the transverse direction. See [30] for full details.

5 ROP Spot Dynamics

Spot location dynamics are depicted in Fig. 12c and d. This location dynamics show attributes governed by the presence of auxin gradient. This characterisation along with instabilities of spot patterns has also been analysed in [31]. To gain further insight, we run a time-step simulation upon taking an unstable boundary stripe solution (labelled by **b** in Fig. 10b) as the initial condition. This computation shows the triggering of a breakup instability, which then gives rise to two spots moving towards domain interior, see Fig. 13. There, the boundary stripe breaks up into two spots (see Fig. 13a) to then slowly drift towards interior (see Fig. 13b). Hence, similarly as in Fig. 12c and d, due to reminiscences of homoclinic snaking, spot formation inherits robusticity traits in 1D addressed in [29].

A wide variety of mixed spot and stripe patterns can be created through breakup instabilities. In order to explore these new types of solution further, we shall perform full numerical continuation of 2D solutions. To do this, we begin with a solution on the stable steady-state branch of Fig. 10. We then continue this solution by varying the main bifurcation auxin overall parameter, both backwards and forwards, to finally obtain the bifurcation diagram depicted in Fig. 14. There, all

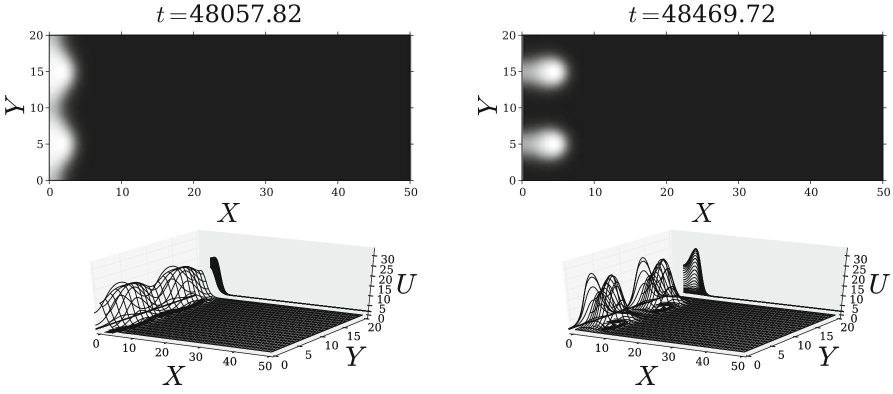

(a) (b)

Fig. 13 Relevant snapshots of transversal instability for unstable boundary stripe **b** in Fig. 10b. (**a**) Break up instability and (**b**) two newly formed boundary spots travelling towards interior. Figures reproduced as well as parameter values from [30]

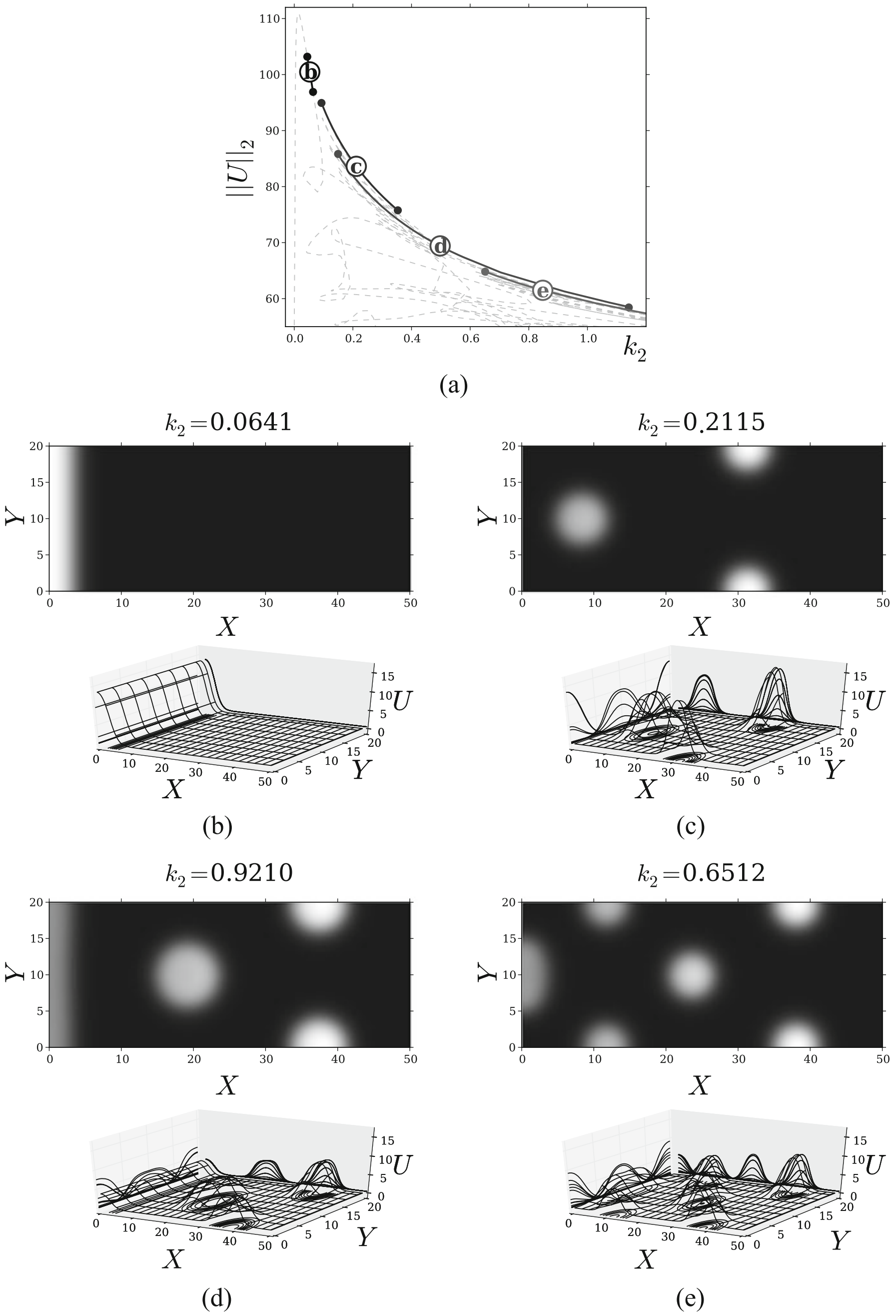

Fig. 14 Bifurcation diagram: spots and a boundary stripe. (**a**) Stable branches are drawn by solid lines and unstable ones by light-grey dashed lines, and filled circles represent fold points. Stable solutions, according to labels (**b**) up to (**e**), are shown in: (**b**) a boundary stripe, (**c**) a spot in the interior and two spots at the boundary, (**d**) a boundary stripe, an interior spot and two spots at the boundary, and (**e**) an interior spot and five spots at the boundary. Figures reproduced as well as parameter values from [30]

unstable branches are plotted as light-grey dashed lines, whereas stable branches are represented as solid lines labelled accordingly as: (b) stable stripes, (c) an interior spot and two spots vertically aligned at the boundary, (d) similar configuration but with an additional stripe, and (e) an interior spot and five spots at the boundary. See Fig. 14b–e for examples of each stable steady-state. In Fig. 14a, as seen before, the bifurcation diagram replicates features studied in the 1D case in [29], such as the overlapping of stable branches of single and multiple localised patches. Stable branches typically become unstable through fold bifurcations. All branches seem to lie on a single connected curve, and no other bifurcations were found except for the pitchfork bifurcations in branch (b). However, branches (c) up to (e) are extremely close to each other and apparently inherit properties from each other.

That is, they seem to undergo a *creation-annihilation cascade* effect similar to that observed in [29]. In other words, take a steady-state which lies on the left-hand end of branch (c) and slide down this branch as auxin overall parameter is increased. It then loses stability at the fold point, and at the other extreme to then fall off in branch (d). Thus a stripe emerges, which pushes the interior spot further in. The same transition follows up to branch (e), more spots arise though as the stripe is destroyed. No further stable branches with steady-states resembling either spots or stripes were found.

Now, in order to derive a 2D solution profiles, we notice that a *conservation principle* is satisfied. Upon assuming radially symmetric N spots, we set evolution operators ∂_t in (4) to zero and find that, in the re-scaled parameter set given in (9)–(10), stationary active-ROP density satisfy that

$$\int_\Omega U_0 \,\mathrm{d}\Omega = \frac{d_y}{\beta\gamma}\,, \quad d_y \equiv \frac{L_y}{L_x}\,,$$

which suggest to re-scale $U = \varepsilon^{-2} U_j$ near each spot, where $j = 1, \ldots, N$. In so doing, we obtain

$$\sum_{j=1}^{N} \int_{\mathbb{R}^2} U_j \,\mathrm{d}\boldsymbol{\xi} \sim \frac{d_y}{\beta\gamma}\,,$$

where $\boldsymbol{\xi} = \varepsilon^{-1}\left(\mathbf{x} - \mathbf{x}_j\right)$. Hence, to properly re-scale system (4) in such a way that a singularly perturbed system is obtained, active- and inactive-ROP densities are re-scaled as follows: $U = \varepsilon^{-2} u$, $V = \varepsilon^{2} v$, and consequently $D = \varepsilon^{-2} D_0$, which comes from balancing Eq. (4b). Due to this, we get a system similar to (8) with dimensionless parameters (9)–(10) in a 2D square domain.

We then define a radial variable $\rho \equiv |\boldsymbol{\xi}|$, and asymptotically expand components u and v with respect to ε. This approach yields two main ingredients:

1. A canonical core problem (CCP) is found at leading order, which solutions u_c and v_c give place to spot solution profiles as given by

$$u_{0j} \equiv \sqrt{\frac{D_0}{\beta\gamma\alpha(\mathbf{x}_j)}}\, u_c\,, \quad v_{0j} \equiv \sqrt{\frac{\beta\gamma}{D_0\alpha(\mathbf{x}_j)}}\, v_c\,.$$

2. Spot location dynamics is given from second order term, which is characterised by a source parameter S_j that satisfies the identity

$$S_j = \frac{\beta\gamma}{D_0}\int_0^\infty \left[\frac{\tau}{\beta}\left(\alpha\left(\mathbf{x}_j\right) u_{0j}^2 v_{0j} - u_{0j}\right) + u_{0j}\right]\rho\, d\rho\,, \quad \text{where}$$

$$S_j = \sqrt{\frac{\beta\gamma}{D_0\alpha(\mathbf{x}_j)}}\, S_{cj}\,. \tag{15}$$

From item 1, profile asymmetric amplitudes are observed to be controlled by auxin gradient. On the other hand, identity in item 2 characterises activation by auxin, longitudinal length and on-and-off switching mechanism in regions close where active-ROP density is high. Notice that τ/β modulates nonlinear terms in (15). These parameters suggests that deactivation rate and removal rate play a relevant key role in auxin catalytic process in 2D. As a consequence, it seems to be an indirect influence of geometrical marks near activation regions.

Upon taking into account these two elements together, we derive a differential algebraic equation (DAE) system which characterises slow N spot dynamics,

$$\frac{d\mathbf{x}_j}{d\eta} = n_1\hat{\boldsymbol{\psi}}_j + n_2\frac{\nabla\alpha(\mathbf{x}_j)}{\alpha(\mathbf{x}_j)}, \quad \hat{\boldsymbol{\psi}}_j \equiv -2\pi\left(S_{cj}\nabla_{\mathbf{x}}R_j + \sum_{i\neq j}^{N} S_{ci}\nabla_{\mathbf{x}}G_{ji}\right), \quad j = 1,\ldots,N\,, \tag{16}$$

where $\eta = \varepsilon^2 t$ is the slow time-scale, R_j is the regular part of Green's function for a square 2D domain and $G_{ji} = G(\mathbf{x}_j;\mathbf{x}_i)$ regulates spots interaction terms. Notice that system (16) consists of two terms: (1) an interaction vector and (2) a kinetic vector. The later consists of the normalised gradient, and the latter deals with interaction between spots, boundary conditions and shape and form of the domain. In addition, the source parameters S_{cj} in (16) satisfy a nonlinear algebraic system, which depends on the instantaneous spatial configuration of the N spots.

In Fig. 15 we compare our full numerical results for the x and y coordinates for the trajectories of two spots, as computed from the RD system (4), and those computed from the corresponding DAE system. The key distinguishing feature in these results is that the spots become aligned to the longitudinal midline of the domain. We observe that the y-components of the spot trajectories are predicted

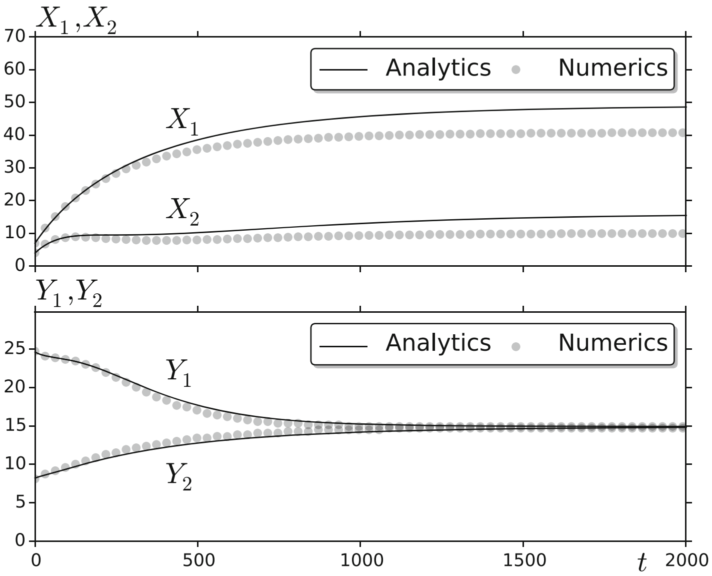

Fig. 15 The time-dependent location of two spots as obtained from system (16) (solid curves). The full numerical results computed from (4) are the filled circles. Observe that the DAE system predicts that the two spots become aligned along the longitudinal midline of the cell. The *x*-coordinate (upper panel) and the *y*-coordinate (bottom panel) of the two spots. Figures reproduced as well as parameter values from [31]

rather accurately over long time intervals by the DAE system. The *x*-components of the trajectories are initially close, but then deviate slightly as *t* increases.

See [31] for a detailed discussion on spot dynamics and other instabilities characterised by auxin on a 2D domain.

6 Concluding Remarks

Auxin is experimentally known to promote RH cell wall swelling. As a consequence, a RH protuberance is then developed at a critical location along the cell and a specific time. The dynamical ingredients for a biochemical interaction as well as auxin catalyst attributes are captured in a model consisting of a non-homogeneous RD system. This model has been proposed by R. Payne and C. Grierson in [9] and thoroughly analysed in [28–31].

We here present a brief review of the key role dynamical features which give place to pattern formation. Nonetheless, from a modelling point of view, our results also provide a setting which may be suitable for precise further experimental designs. On the other hand, pattern formation theory still remains in darkness; we here depict all essential dynamical components that rigorously characterise localised solutions, as well as location dynamics controlled by the auxin gradient. Other instabilities arising in 1D and 2D are not here addressed. Nonetheless, features considered can be summarised as follows:

- Turing subcritical bifurcations favours localised solutions; as a consequence, they determine the onset of localised stationary solutions that are organised in a homoclinic snaking fashion.
- Due to reminiscences of homoclinic snaking, as auxin gradient is included as a biochemical accelerator, a strong slanted overlapping of stable branches, which are flaked by fold bifurcations, give rise to hysteretical behaviour.
- Amplitude asymmetry and location are controlled by auxin gradient, where physical features as shape and form are more relevant when a 2D domain is taken into account.
- Although not discussed here, the key instabilities that regulate transitions between family of localised patterns are: (1) competition instability and (2) peanut-splitting instability. The former can be understood as an under-crowding instability which determines whether a pattern consisting of multi-localised structures persists on a $\mathcal{O}(1)$ time scale; on the contrary, the latter works as a over-crowding instability, which promotes nonlinear events yielding spot self-replication. In both cases, a threshold is passed to trigger such an instabilities. These thresholds deal with a strong relationship between auxin and length of the domain.

Notice that there still are physical and biological features not yet considered. These may be other transport processes, geometrical characteristics as torsion and curvature, and a collection of non-RH and RH cells all together with an auxin flux catalysing pattern formation in *Arabidopsis thaliana*.

Acknowledgements I specially thank D. Avitabile, A. Champneys, C. Grierson and M. Ward who have travelled along my side on this dynamical journey. Also, my thanks to the organisers of the Biological Physics Mexico City 2017 Conference for the well-organised meeting. This research has partially been supported by UNAM–PAPIIT grant IA104316–RA104316 (Mexico).

References

1. Grierson C, Nielsen E, Ketelaarc T, Schiefelbein J (2014) Root hairs: the Arabidopsis book 11. American Society of Plant Biologists, Rockville, MD
2. Berger F, Hung C, Dolan L, Schiefelbein J (1998) Control of cell division in the root epidermis of Arabidopsis thaliana. Dev Biol 194:235–245
3. Jones A, Kramer E, Knox K, Swarup R, Bennett M, Lazary C, Leyser HO, Grierson C (2009) Auxin transport through non-hair cells sustains root-hair development. Nat Cell Biol 11:78–84
4. Nagawa S, Xu T, Yang Z (2010) Rho GTPases in plants: conservation and invention of regulators and effectors. Small GTPases 1:78–88
5. Bustelo X, Sauzeau V, Berenjeno I (2007) GTP-binding proteins of the Rho/Rac family: regulation, effectors and functions in vivo. Bioessays 29:356–370

6. Geldner N, Anders N, Wolters H, Keicher J, Kornberger W, Muller P, Delbarre A, Ueda T, Nakano A, Jüngens G (2003) The Arabidopsis GNOM ARF-GEF mediates endosomal recycling, auxin transport, and auxin-dependent plant growth. Cell 112:219–230
7. Mori Y, Jilkine A, Edelstein-Keschet L (2008) Wave-pinning and cell polarity from a bistable reaction-diffusion system. Biophys J 94:3684–3697
8. Breña-Medina VF (2013) Modelling initiation of plant root hairs; a reaction-diffusion system in a non-homogenous environment. PhD thesis, University of Bristol
9. Payne R, Grierson C (2009) A theoretical model for ROP localisation by auxin in Arabidopsis root hair cells. PLoS One 4:e8337. https://doi.org/10.1371/journal.pone.0008337
10. Kramer EM, Rutschow HL, Mabie SS (2011) AuxV: a database of auxin transport velocities. Trends Plant Sci 16:461–463
11. Kramer EM (2004) PIN and AUX/LAX proteins: their role in auxin accumulation. Trends Plant Sci 9:578–582
12. Grierson C et al (2009) Root Development Lab, School of Biological Sciences – University of Bristol
13. Sorek N, Gutman O, Bar E, Abu-Abied M, Feng X, Running M, Lewinsohn E, Ori N, Sadot E, Henis Y, Yalovsky S (2011) Differential effects of prenylation and S-acylation on type I and II ROPs membrane interaction and function. Plant Physiol 155:706–720
14. Jilkine A, Maree A, Edelstein-Keschet L (2007) Mathematical model for spatial segregation of the Rho-family GTPases based on inhibitory crosstalk. Bull Math Biol 69:1943–1978
15. Otsuji M, Ishihara S, Co C, Kaibuchi K, Mochizuki A (2007) A mass conserved reaction-diffusion system captures properties of cell polarity. PLoS Comput Biol 3:e108
16. Schnakenberg J (1979) Simple chemical reaction systems with limit cycle behaviour. J Theor Biol 81:389–400
17. Nicolis G, Prigogine I (1977) Self-organization in nonequilibrium systems. Wiley-Interscience, New York
18. Maini PK, Painter KJ, Phong-Chau HN (1997) Spatial pattern formation in chemical and biological systems. J Chem Soc Faraday Trans 93:3601–3610
19. Ward MJ, Wei J (2002) The existence and stability of asymmetric spike patterns for the Schnakenberg model. Stud Appl Math 109:229–264
20. Iron D, Wei J, Winter M (2004) Stability analysis of Turing patterns generated by the Schnakenberg model. J Math Biol 49:358–390
21. Kolokolnikov T, Ward M, Wei J (2009) Spot self-replication and dynamics for the Schnakenberg model in a two-dimensional domain. J Nonlinear Sci 19:1–56
22. Dufiet V, Boissonade J (1992) Conventional and unconventional Turing patterns. J Chem Phys 96:662–673
23. Lin F, Du Q (1997) Ginzburg-Landau vortices: dynamics, pinning, and hysteresis. SIAM J Math Anal 28:1265–1293
24. Ward M, Mcinerney D, Houston P, Gavaghan D, Maini P (2002) The dynamics and pinning of a spike for a reaction-diffusion system. SIAM J Appl Math 62:1297–1328
25. Maini PK, Benson DL, Sherrat JA (1992) Pattern formation in reaction-diffusion models with spatially inhomogeneous diffusion coefficients. IMA J Math Appl Med Biol 9:197–213
26. Holloway DM, Harrison LG (1995) Order and localization in reaction-diffusion pattern. Phys A Stat Mech Appl 222:210–233
27. Hunding A (1985) Morphogen prepatterns during mitosis and cytokinesis in flattened cells: three dimensional Turing structures of reaction-diffusion systems in cylindrical coordinates. J Theor Biol 114:571–588
28. Breña-Medina V, Champneys AR (2014) Subcritical Turing bifurcation and the morphogenesis of localized structures. Phys Rev E 90:032923
29. Breña-Medina V, Champneys AR, Grierson C, Ward MJ (2014) Mathematical modelling of plant root hair initiation; dynamics of localized patches. SIAM J Appl Dyn Syst 13:210–248
30. Breña-Medina V, Avitabile D, Champneys A, Ward M (2015) Stripe to spot transition in a plant root hair initiation model. SIAM J Appl Math 75:1090–1119

31. Avitabile D, Breña-Medina V, Ward MJ (2017) Spot dynamics in a reaction-diffusion model of plant root hair initiation. arXiv:1703.02608 and bioRxiv:114876
32. Murray J (2002) Mathematical biology II: spatial models and biomedical applications, 3rd edn. Springer, New York
33. Beck M, Knobloch J, Lloyd DJB, Sandstede B, Wagenknecht T (2009) Snakes, Ladders, and Isolas of localized patterns. SIAM J Math Anal 41:936–972
34. Woods PD, Champneys AR (1999) Heteroclinic tangles and homoclinic snaking in the unfolding of a degenerate reversible Hamiltonian-Hopf bifurcation. Physica D 129:147–170
35. Avitabile D, Lloyd D, Burke J, Knobloch E, Sandstede B (2010) To snake or not to snake in the planar Swift-Hohenberg equation. SIAM J Appl Dyn Syst 9:704–733
36. Grieneisen V, Maree A, Hogeweg P, Scheres B (2007) Auxin transport is sufficient to generate a maximum and gradient guiding root growth. Nature 449:1008–1013
37. Doelman A, van der Ploeg H (2002) Homoclinic stripe patterns. SIAM J Appl Dyn Syst 1: 65–104